A Metal–Insulator Transition of the Buried MnO_2 Monolayer in Complex Oxide Heterostructure

Heng-Jui Liu, Jheng-Cyuan Lin, Yue-Wen Fang, Jing-Ching Wang, Bo-Chao Huang, Xiang Gao, Rong Huang, Philip R. Dean, Peter D. Hatton, Yi-Ying Chin, Hong-Ji Lin, Chien-Te Chen, Yuichi Ikuhara, Ya-Ping Chiu, Chia-Seng Chang, Chun-Gang Duan, Qing He, and Ying-Hao Chu**

Due to the interplay of lattice, charge, orbital, and spin degrees of freedom, strongly correlated electron systems in complex oxides generate a rich spectrum of competing phases and emergent physics.[1,2] Recently, extensive studies suggest that complex oxide interfaces provide a powerful route to manipulate these degrees of freedom and offer new possibilities for next generation devices, thus create a new playground for investigating novel physics and the emergence of fascinating states in condensed matter.[3–5] In 2004, a 2D electron gas was discovered at the $LaAlO_3/SrTiO_3$ (LAO/STO) heterointerface.[6] Since then, the LAO/STO interface shows ultrahigh mobility, interface superconductivity,[7] magnetoresistance,[8] and multiple tunable properties.[9–11] On the other hand, the discovery of free-standing 2D materials has inspired the research for exploring new low-dimensional materials.[12–14] Pioneered by graphene,[15] these 2D materials exhibit aboundant unusual physical phenomena that are undiscovered in bulk forms. The confinement of charge and heat transport at such ultrathin planes offers possibilities to overcome the bottleneck of current devices. Interestingly, in complex oxides, the physical properties have usually been dominated by their 2D structural units, the metal-oxide planes. For example, the CuO_2 plane in $YBa_2Cu_3O_{7-x}$,[16] or the RuO_2 plane in Sr_2RuO_4 is responsible for their superconductivity.[17] However, most studies about understanding the contribution of such oxide planes on the corresponding properties still concentrate on the viewpoint from their macroscopic behaviors in bulk materials. Therefore, to create and manipulate a single metal-oxide plane would provide other solutions for realizing the fundamental physics of the strongly correlated electron systems. Researchers have speculated that superior properties such as high temperature superconductivity and high mobility electronic transport can occur at an oxide plane. Gozar et al. have proposed that a single CuO_2 plane with a superconducting temperature ranging from 15–50 K could be procured at the interface between metallic $La_{1.55}Sr_{0.45}CuO_4$ and insulating La_2CuO_4.[18] Moreover, Chen et al. have also demonstrated that an insertion of one unit cell $La_{1-x}Sr_xMnO_3$ (x = 0, 1/8, and 1/3) insulating layer between disordered LAO and crystalline STO enhances the electron mobility by more than two orders of magnitude.[19]

In this study, we attempted to create a single metal-oxide plane as a 2D monolayer through interface engineering. This 2D oxide monolayer can be obtained at the heterostructure similar to the case of a single-unit-cell manganite ultrathin film sandwiched between two neighboring complex oxides.[19] In such heterostructures, the intrinsic properties of 2D oxide

Dr. H.-J. Liu, Prof. Y.-H. Chu
Department of Materials Science and Engineering
National Chiao Tung University
Hsinchu 30010, Taiwan
E-mail: yhc@nctu.edu.tw
Dr. H.-J. Liu, Prof. Y.-P. Chiu
Department of Physics
National Taiwan Normal University
Taipei 11677, Taiwan
J.-C. Lin, Dr. B.-C. Huang, Prof. Y.-H. Chu, Prof. C.-S. Chang
Institute of Physics
Academia Sinica
Taipei 11529, Taiwan
Dr. Y.-W. Fang, Prof. R. Huang, Prof. C.-G. Duan
Key Laboratory of Polar Materials and Devices
Ministry of Education
East China Normal University
Shanghai 200241, China
J.-C. Wang, Prof. Y.-P. Chiu
Department of Physics
National Sun Yat-sen University
Kaohsiung 80424, Taiwan
Dr. X. Gao, Prof. R. Huang, Prof. Y. Ikuhara
Nanostructures Research Laboratory
Japan Fine Ceramics Center
Nagoya 456-8587, Japan
P. R. Dean, Prof. P. D. Hatton, Prof. Q. He
Department of Physics
Durham University
Durham DH1 3LE, UK
E-mail: qing.he@durham.ac.uk
Dr. Y.-Y. Chin, Dr. H.-J. Lin, Dr. C.-T. Chen
National Synchrotron Radiation Research Center
Hsinchu 30076, Taiwan
Prof. Y. Ikuhara
Institute of Engineering Innovation
The University of Tokyo
Tokyo 113-8656, Japan

DOI: 10.1002/adma.201602281

© 2016 WILEY-VCH Verlag GmbH & Co. KGaA, Weinheim

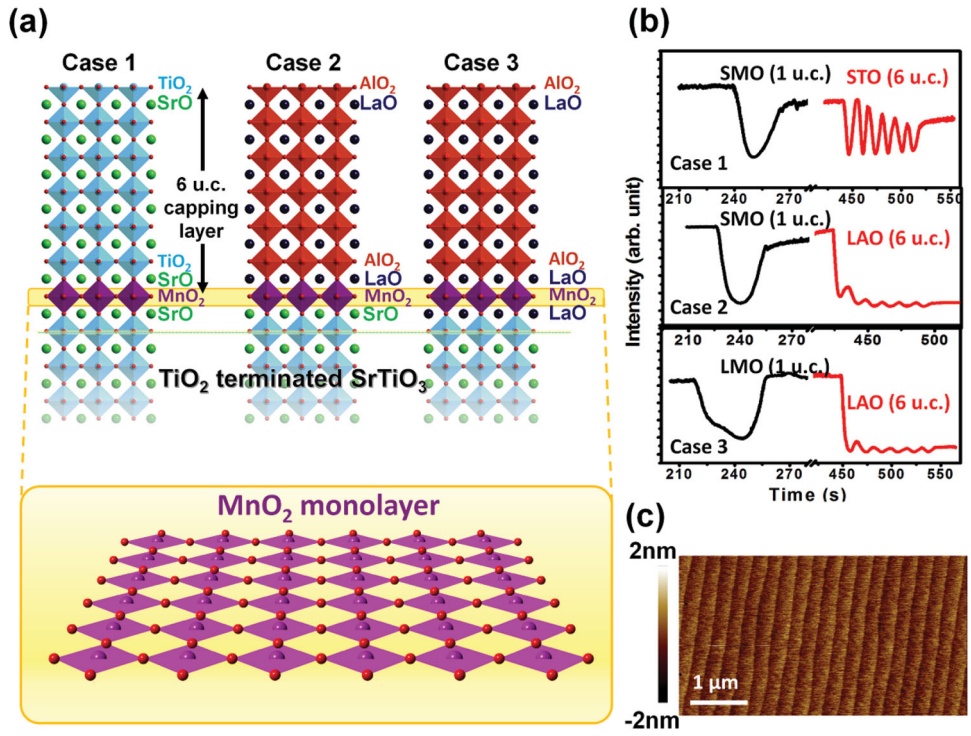

Figure 1. a) Schematics of the designed MnO_2 monolayers with different electrostatic boundary conditions. case 1: $SrO^0/MnO_2/SrO^0$, case 2: $LaO^+/MnO_2/SrO^0$, case 3: $LaO^+/MnO_2/LaO^+$. b) Real time monitoring of RHEED intensity for these three cases. Case 1: 1 unit cell of SMO grown on TiO_2 terminated STO capped with 6 unit cells of STO. Case 2: 1 unit cell of SMO grown on TiO_2 terminated STO capped with 6 unit cells of LAO. Case 3: 1 unit cell of LMO grown on TiO_2 terminated STO capped with 6 unit cells of LAO. c) The typical morphology of atomically flat surface for these three cases.

monolayer can provide a basic understanding of the physics on the dimensionality-confined strongly correlated electron systems. This study delivers a generic approach to study the dimensional confinement of strongly correlated electron systems and provides a direction to design new electronic devices.

The design concept is illustrated in **Figure 1**a, where a transition metal-oxide monolayer is buried in complex oxide heterostructures. The MnO_2 monolayer has been chosen as a model system since the mixture of Mn^{4+} and Mn^{3+} cations in these oxide planes dominate the novel physical phenomena of colossal magnetoresistance manganites.[20–22] To systematically modulate this MnO_2 monolayer, three heterostructures are studied in parallel. In case 1, the MnO_2 monolayer is embedded into a STO crystal, such that the top and bottom neighboring layers of the MnO_2 monolayer are both SrO. Because of the charge neutrality of SrO layers, the valence state of Mn cations is expected to be +4, in which their 3*d* electrons fill up to the t_{2g} orbitals. In case 2, the MnO_2 monolayer is inserted into a LAO/STO heterointerface. The top neighbor layer of the MnO_2 monolayer is LaO^+ and the bottom neighbor layer is SrO. The charge transfer is expected to drive the valence state of Mn cations between +3 and +4. Thus, the extra 3*d* electrons start to fill into e_g orbitals. The design concept of case 3 is similar to case 2, but going further. In this structure, both the top and bottom neighbor layers of the MnO_2 monolayer are designed to be LaO^+. The valence state of Mn cations, in this case, should be pushed further toward +2, resulting in a mixture of multivalence Mn cations.

To prepare such MnO_2 monolayers described above, the layer-by-layer growth technique through pulsed laser deposition (PLD) equipped with a high-pressure reflection high energy electron diffraction (RHEED) facility was adopted. Single TiO_2-terminated (001) STO substrates[23] are the prerequisites for obtaining the layer-by-layer growth and precisely controlling surface termination of subsequent layers. According to the RHEED principle, when a full period of intensity oscillation finished by first decreasing to the minimum and then coming back to the maximum indicates the completion of one atomic layer satisfying the chemical composition and electrical neutrality, namely, one unit-cell thick layer here.[24–26] Simultaneously, it also implies that surface has formed a new single termination from the subsequently deposited film. For instance, in case 1, while one unit cell of $SrMnO_3$ (SMO) layer has been deposited onto TiO_2 terminated STO substrate, the SrO plane naturally connects to the TiO_2 termination, making the MnO_2 plane as the new termination on the surface for keeping the structure continuity. Thereafter, this new termination has been covered by six-unit cell STO film. Hence, this heterostructure now looks like a MnO_2 monolayer inserted in the STO single crystal. Here we can observe one complete oscillation of SMO (in black) and six complete oscillations of STO (in red) in RHEED intensity spectrum as the top panel in Figure 1b, which confirms the desired architecture of case 1. In case 2, the one unit cell of SMO layer has been kept but the capping layer is replaced by six unit cells of LAO. In case 3, unlike the MnO_2 monolayers possessing electronic neutrality in case 1,

© 2016 WILEY-VCH Verlag GmbH & Co. KGaA, Weinheim

Table 1. Results of total energy calculations using U^{eff}_{Mn} = 4.5 eV. FM and AFM denote the ferromagnetic and antiferromagnetic configurations of the monolayer MnO_2 in each case.

	FM [eV]	AFM [eV]	FM-AFM [meV]/(Mn–Mn pair)
Case 1	−1126.46(9)	−1126.54(6)	19.3
Case 2	−1127.42(9)	−1127.31(4)	−28.6
Case 3	−1139.06(8)	−1138.68(9)	−94.7

the polar MnO_2 monolayer in case 3 is developed by growing one unit cell of $LaMnO_3$ (LMO) layer, and then covered by six unit cells of LAO. For case 2 and case 3, both RHEED intensity profiles show the similar behavior to that of case 1. However, the oscillations during the growth of LAO capping layer exhibit a quick drop of the intensity at the beginning three unit cells. Such drop of intensity in RHEED oscillations can be ascribed to the surface structural reconstruction due to large lattice mismatch between STO and LAO. After that, a stable oscillatory intensity can be observed, substantiating a high quality of LAO epitaxial thin film. The surfaces of all heterostructures were then inspected by atomic force microscopy (AFM), where the morphologies remain atomically smooth as the typical image shown in Figure 1c.

Because the charge transfer is expected to emerge and modify the electronic and magnetic structures of the MnO_2 monolayers, a question arises: what are the magnetic ground states of the MnO_2 monolayers in these cases? To address this question, we employed the density functional theory (DFT) method to perform total-energy calculations for the heterostructures. Several different Hubbard U^{eff}_{Mn} values of 2, 4, 4.5, and 7 eV were tested in calculations. Here U^{eff}_{Mn} = 4.5 eV has been chosen as the representative since this value was previously obtained for bulk $LaMnO_3$[27] using the linear response approach of Cococcioni and Gironcoli.[28] However, the robustness of magnetic ground states for the three cases is also guaranteed in the calculations with U^{eff}_{Mn} = 2 and 4 eV, except for the extraordinarily large U = 7 eV (more details are revealed in the Experimental Section: DFT calculation for details and Table S1, Supporting Information). The results of the respective total energies for each case in ferro/antiferro-magnetic configuration are listed in **Table 1** using U^{eff}_{Mn} = 4.5 eV. One can clearly see that Mn–Mn pair in case 1 exhibits antiferromagnetic coupling, whereas ferromagnetism is stabilized in the ground state for case 2 and case 3. Due to the significant difference in the magnetic ground state, a dramatic difference in electronic structures of these heterostructures can be expected. We then computed the electronic structures of the heterostructures and presented the obtained density of states (DOS) extracted from spin-polarized calculations with U^{eff}_{Mn} = 4.5 eV in **Figure 2**. From the total DOS, it is clear that case 1 is an insulator with an energy gap of at least 0.5 eV and case 3 is a metal with the Fermi level shifted to the conduction bands of both spin channels. However, case 2 is

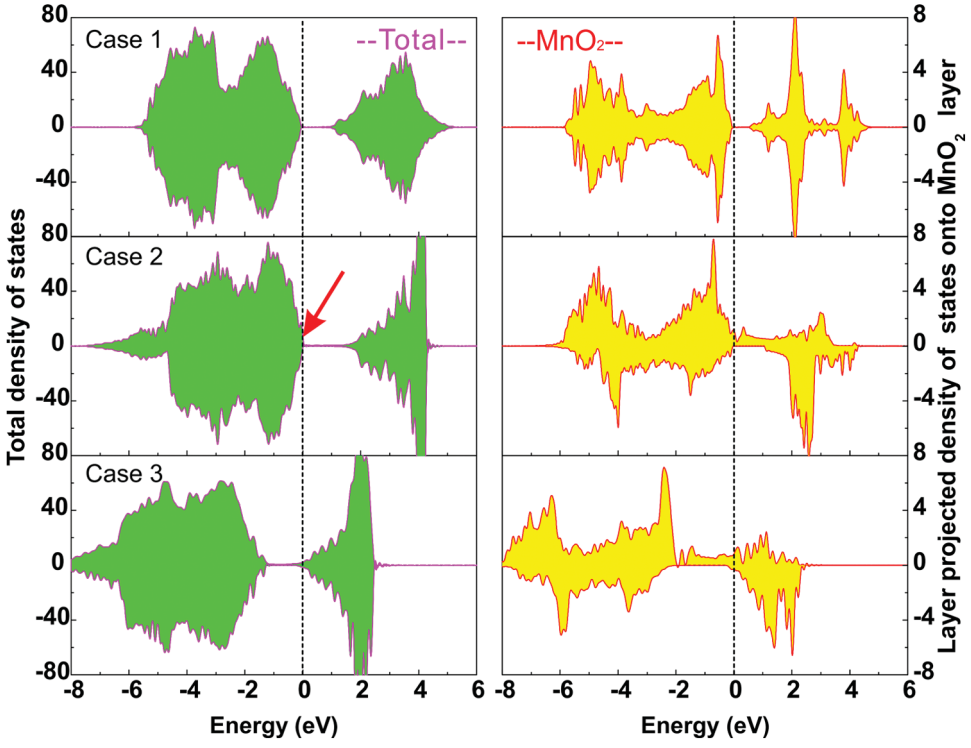

Figure 2. Density of states of the heterostructures: The left panel shows the total DOS of each case and the right panel shows the layer projected DOS for MnO_2 layer in corresponding case. Zero is the reference for the Fermi level. The DOS at the Fermi level in case 2 pointed by a red arrow must be given a particular attention because it actually displays half-metallic conductivity in DFT calculations which is shown in the right panel. Here, total DOS represents the density of states of the whole heterostructure model, and layer projected DOS stands for the density of states of the monolayer MnO_2 in each case.

© 2016 WILEY-VCH Verlag GmbH & Co. KGaA, Weinheim

more complicated. It seems to be an insulator since the total DOS (middle left panel of Figure 2) is analogous to case 1. However, from the projected DOS of the MnO_2 layer, as shown in the middle right panel of Figure 2, one can see that case 2 indeed displays a half-metallicity with an energy gap of about 0.53 eV in the minority spin channel. It should be noted that the Fermi level shifts up gradually from case 1 to case 2 to case 3, indicating an increasing electronic occupation of Mn cations in these heterostructures. We hence conducted the analysis of Bader charge for Mn cations in each case, and found that the valence state of Mn cations meets the relationship of case 1 > case 2 > case 3. We further examined the electronic charge by integrating the Mn 3*d* orbital resolved DOS. The electronic charge of Mn in each case is 4.73, 4.80, and 4.83, respectively. These semiquantitative results clearly show charge transfer really occurs, and the oxidization state of Mn in case 1 (3) is the biggest (smallest) one among the three cases.

High-angle annular dark-field scanning transmission electron microscopy (HAADF-STEM) was carried out to examine the validity of these heterostructures. **Figure 3** shows the typical

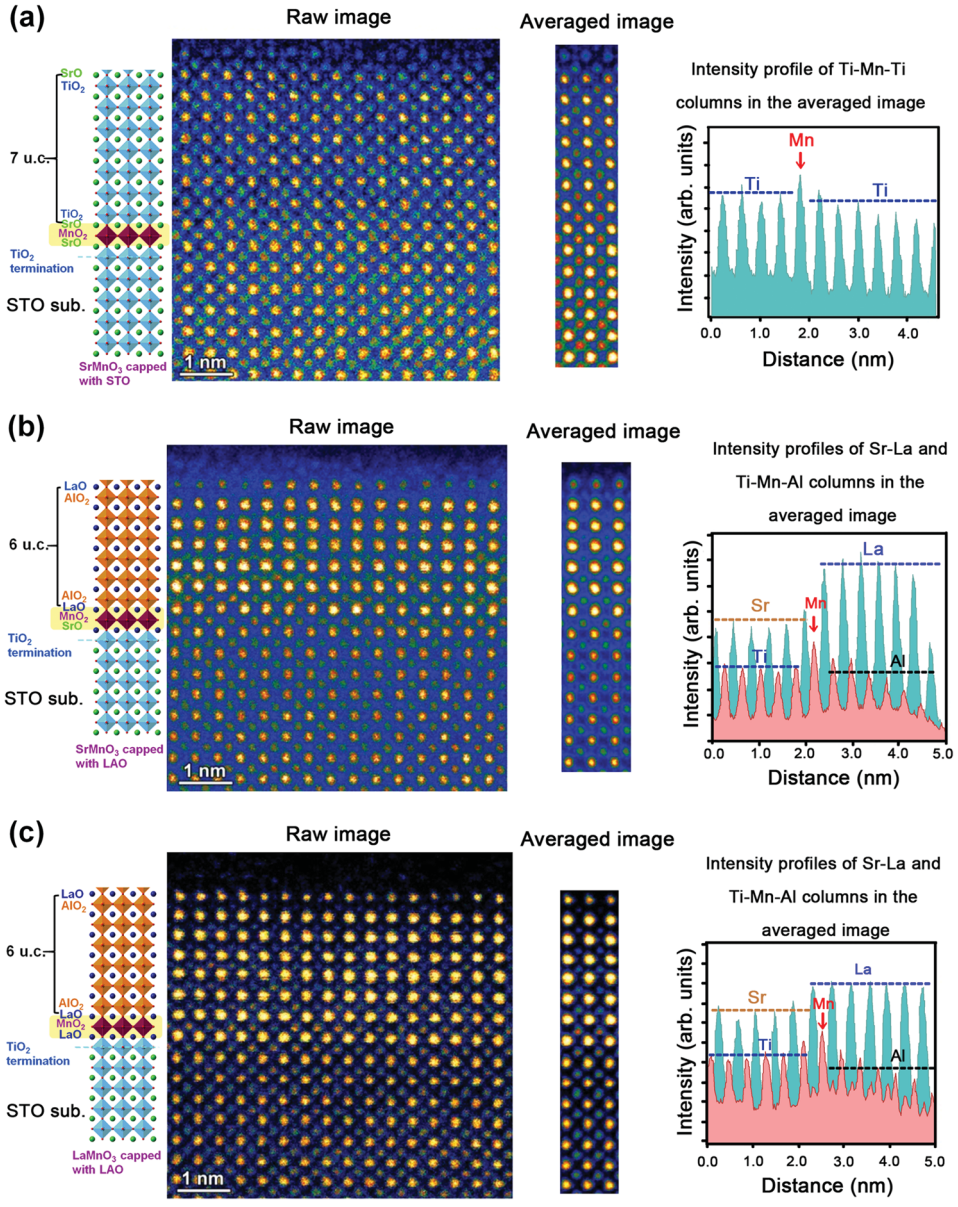

Figure 3. Typical HAADF-STEM images of the three MnO_2 monolayer samples. a) Raw image (left), averaged image (middle) and the intensity profiles of the Ti–Mn columns (right) in the averaged image of the SMO monolayer capped with 6 unit cells of STO observed along the [010] zone axis of STO substrate. b) Raw image (left), averaged image (middle) and the intensity profiles of the Sr–La and Ti–Mn–Al columns (right) in the averaged image of the SMO monolayer capped with 6 unit cells of LAO observed along the [010] zone axis of STO substrate. c) Raw image (left), averaged image (middle) and the intensity profiles of the Sr–La and Ti–Mn–Al columns (right) in the averaged image of the LMO monolayer capped with 6 unit cells of LAO observed along the [010] zone axis of STO substrate.

© 2016 WILEY-VCH Verlag GmbH & Co. KGaA, Weinheim

HAADF-STEM images of case 1, 2, and 3 along the [010] direction of the STO substrate. The atomic columns of A sites (Sr and La) and B sites (Ti, Mn, and Al) can be seen in the raw image, as shown in the left panel of Figure 3. Because the atomic number of La (Z = 57) is much larger than that of Sr (Z = 38), both atomic columns can be distinguished unambiguously. The columns of La exhibit brighter contrast than those of Sr. However, the columns of the Mn monolayer are very difficult to be differentiated from those of Ti due to a small difference in their atomic numbers of Mn (Z = 25) and Ti (Z = 22). The difference in the contrast between Mn and Ti is almost comparable to the noise level in the raw image. To improve the signal-to-noise ratio of the raw image, an average process has been performed, as shown in the middle of Figure 3a. In the averaged image, the heavier Mn columns exhibit relatively brighter contrast than the lighter Ti columns, as revealed in the intensity profile of the Ti–Mn–Ti columns, shown in the right panel of Figure 3a. The existence of the MnO_2 monolayer is more clearly revealed when one compares the intensity profiles of the Sr–La columns and the Ti–Mn–Al columns in case 2 and case 3. Especially, the different sequence of the MnO_2 monolayer and the LaO layer show a very obvious intensity variation as shown in right panels of Figure 3b,c, respectively. Furthermore, we have found that slight interdiffusion of cations occurs in the cases with LAO capping layer according to the HAADF-STEM observations. For example, in the case 2, few Mn cations diffuse into the neighboring layers, and rare La cations diffuse into the STO substrate as revealed by atomic-resolution EDS mapping as presented in the Supporting Information (Figure S1). Similar phenomena have been observed in the case 3 as well. These results of interfacial chemical composition identification imply that although the manganite monolayer has limited intermixing of Mn cations into neighboring layers, it also effectively hinders the interdiffusion of La cations across the interface.

Soft X-ray absorption based techniques are ideal tools to provide chemical, electronic, and magnetic information of these MnO_2 monolayers, as they are inherently element-specific, allowing the characterization of the valence states and the symmetry of individual lattice sites.[29–31] **Figure 4**a shows the X-ray absorption spectra (XAS) across the Mn *L*-edges taken from the heterostructures. The changes of the XAS among various cases provide a direct evidence of the change in the valence state of Mn cations. For comparison, three reference spectra for Mn^{4+} (SMO), Mn^{3+} (LMO), and Mn^{2+} (MnO) cations are added in the upper part of Figure 4a. Three dashed lines in this figure indicate the peak position of signature absorption for Mn^{4+}, Mn^{3+}, and Mn^{2+} cations. The corresponding signature peaks of the MnO_2 monolayers for the three cases can be observed in the XAS, suggesting a systematic change of the valence state of Mn cations. In case 1, the valence state of Mn cations is dominated by Mn^{4+} cations. In case 2, a mixed valence state of Mn^{3+}

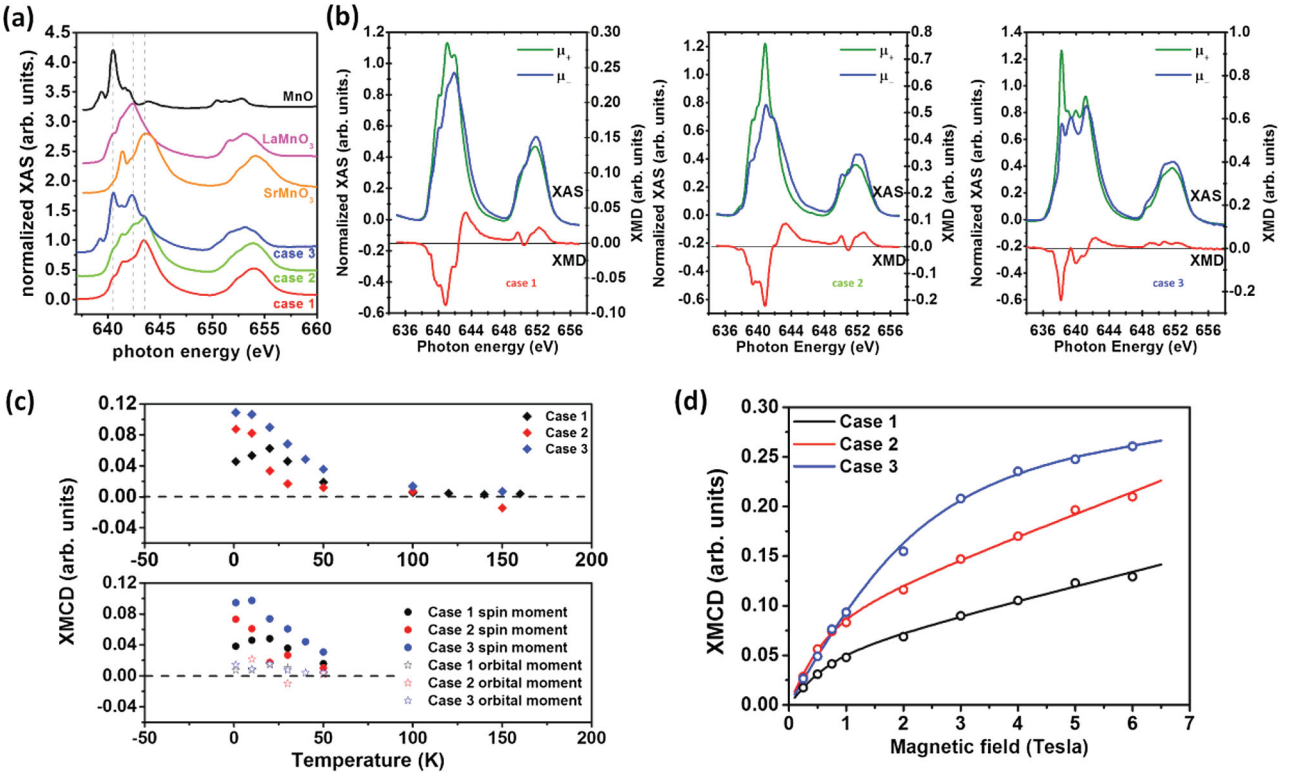

Figure 4. a) The XAS spectra across the Mn *L*-edges taken from the MnO monolayers with various electrostatic boundary conditions. b) The XMCD spectra across the Mn *L*-edges taken from the MnO_2 monolayers with various electrostatic boundary conditions. c) The extracted orbital and spin moments of the MnO_2 monolayers based on sum rules as a function of temperature with various electrostatic boundary conditions. d) The XMCD signal of the MnO_2 monolayers as a function of magnetic field with various electrostatic boundary conditions.

© 2016 WILEY-VCH Verlag GmbH & Co. KGaA, Weinheim

and Mn^{4+} is detected. Further, in case 3, the valence state of Mn cations is dominated by a mixture of Mn^{+2} and Mn^{3+}. We also estimated the amount of charge transfer from the capping layers to the MnO_2 monolayer by using the weighted curves of adequate proportion of SMO, LMO, and MnO reference spectra as shown in Figure S2 of the Supported Information. In case 1, no apparent charge transfer is observed because of charge neutrality in both STO capping layer and STO substrate, consistent with the expected valence of Mn^{4+}. In case 2 and case 3, the best weighted spectra of LMO (Mn^{3+})/SMO (Mn^{4+}) = 40/60 and MnO_2 (Mn^{2+})/LMO (Mn^{3+}) = 43/57 are obtained, respectively. Therefore, the mixed valence of Mn cations in case 2 and case 3 can be estimated as around +3.6 and +2.57. Namely, the amount of charge transfer from LAO capping layer are around 0.4 electron in case 2 and 0.43 electron in case 3, respectively. As suggested by the DFT calculation, we further investigated the magnetic states of these MnO_2 monolayers. Thus, X-ray magnetic circular dichroism (XMCD) measurements across the Mn *L*-edges as a function of magnetic field and temperature were employed to probe the magnetic phases and possible phase transitions.

Figure 4b shows the XMCD spectra of the heterostructures measured at ≈3 K with an applied magnetic field of ≈6 T. Significant differences in both magnitudes and line shapes of XMCD spectra in these MnO_2 monolayer were found. The smallest XMCD was detected in case 1, while case 3 showed the largest XMCD, indicating a stronger magnetic response of case 3. In order to obtain quantitative magnetometry, sum rules were applied to the XAS-XMCD spectra to extract the spin moment and orbital moment of Mn cations shown in Figure 4c. The magnitude of orbital moment in these samples is found to be very close and shows very little temperature dependence, which is consistent with the expectation. This is because the origin of orbital magnetic moment comes from the orbital motion of electrons. In most 3*d* tranistion metal oxides, the orbital moment is aligned when a magnetic field is applied. Therefore, a temperature independence is highly expected since it is a signature of atoms. Of course, in oxide heterostructures, the lattice–orbit coupling sometimes could become significant. For example, a strong crystal field and the Jahn–Teller (JT) distortion in $SrMnO_3$ or $LaMnO_3$ lead to orbital degeneracy accompanying with preferred electron occupancy and ordering. Such systems may show temperature dependent orbital moment. In our current study, these MnO_2 monolayers are almost fully constrained by the STO substrates, of which the lattice variation is around 0.2% while decreasing temperature from room temperature to 10 K (the thermal expansion of STO is around 2.8×10^{-5} Å K^{-1}).[32] Such a slight change of lattice is supposed to cause a little variation on orbital preference. Hence, a constant magnetic field and lattice confinement can be responsible for nearly temperature independent orbital moment in these MnO_2 monolayers. On the other hand, the spin moment of case 3 shows the largest magnitude and a clear temperature dependence with a transition around 60 K. Similar behavior can be found in other two cases as well (the way to determine this transition temperature is exhibited in Figure S3, Supporting Information). It implies that the spin moment dominates the magnetic transition in these monolayer systems. Besides, the magnetic-field dependent XMCD curves measured along out-of-plane direction at ≈3 K are shown in Figure 4d, where a curve fitting based on superparamagnetism with Langevin function[33] can be used to fit the field dependent magnetic behavior for all samples. These results suggest that these systems possess high magnetic susceptibility and paramagnetic-like feature under a very finite size (within one unit-cell manganite ultrathin film), clearly indicating a nature of 2D magnetism. It has been known that an exchange interaction, such as super exchange or double exchange, is required to develop the origin of magnetism in transition metal oxides. Specifically, the orbital direction should be the crucial factor to determine the interaction to be ferromagnetic or antiferromagnetic, which can be revealed by X-ray magnetic linear dichroism (XMLD). In our systems, the clear XMLD signals were detected, suggesting a preference of the orbital direction (Figure S4, Supporting Information). However, a long range order is easier to be formed in a 3D system than in a 2D one, within which only one atomic plane can be used to establish the long-range correlation. That means in a 2D quantum confined system, the material is more difficult, sometimes impossible, to form magnetic domains with stable sizes. Therefore, this 2D behavior of a superparamagnetic state can be ascribed to the formation of nanoscale domain-like area while lowering the temperature. Based on the results of XAS related techniques, the electronic and magnetic structures of the MnO_2 monolayers can be manipulated by a careful control of the electrostatic configurations.

In order to probe the electronic structure of these MnO_2 monolayers in real space, the cross-sectional scanning tunneling microscopy and spectroscopy (XSTM/XSTS) was carried out on the surface of cleaved samples in an ultrahigh vacuum (UHV) chamber.[34] The schematic of XSTM measurements of case 1 and case 3 are illustrated in **Figure 5**a. This technique can provide the information of local density of states (LDOS) spatially with atomic-level resolution. Figure 5b shows the typical STM topography across the heterointerfaces of case 1 and case 3 with applied voltage of –2.0 V. Various regions can be distinguished based on the specific spectra among different layers. The corresponding spectroscopic results for the heterostructures of case 1 and case 3 are shown in Figure 5c. Compared to the local electronic information of case 1 under +1.5 V at 110 K, a dramatically enhanced electronic signal was observed at the interface of case 3, revealing the critical signature of the electronic structures at the MnO_2 monolayer of case 3. Furthermore, the evolution of the band alignment across heterointerfaces of case 1 and case 3 was quantitatively built and mapped shown in Figure 5d,e to illustrate the trivial discrepancy in the electronic structure. Based on the spectroscopic data, the energy gap of the MnO_2 monolayer in case 1 is about 0.4 eV, whereas the energy gap of the MnO_2 monolayer is about 1.6 eV in case 3, showing that the MnO_2 monolayers in these cases are semiconducting. According to our DFT calculation, the LDOS of case 1 at 110 K shows good agreement with the theory in Figure 2, where its semiconducting properties with a small energy gap are well reproduced. However, the LDOS of case 3 at 110 K has a larger energy gap, which is different from the theoretical prediction. This discrepancy can be attributed to the thermal effect at the experimental temperature (110 K); while, the DFT prediction is based on the calculations of the system ground state at 0 K. To prove this speculation, the

© 2016 WILEY-VCH Verlag GmbH & Co. KGaA, Weinheim

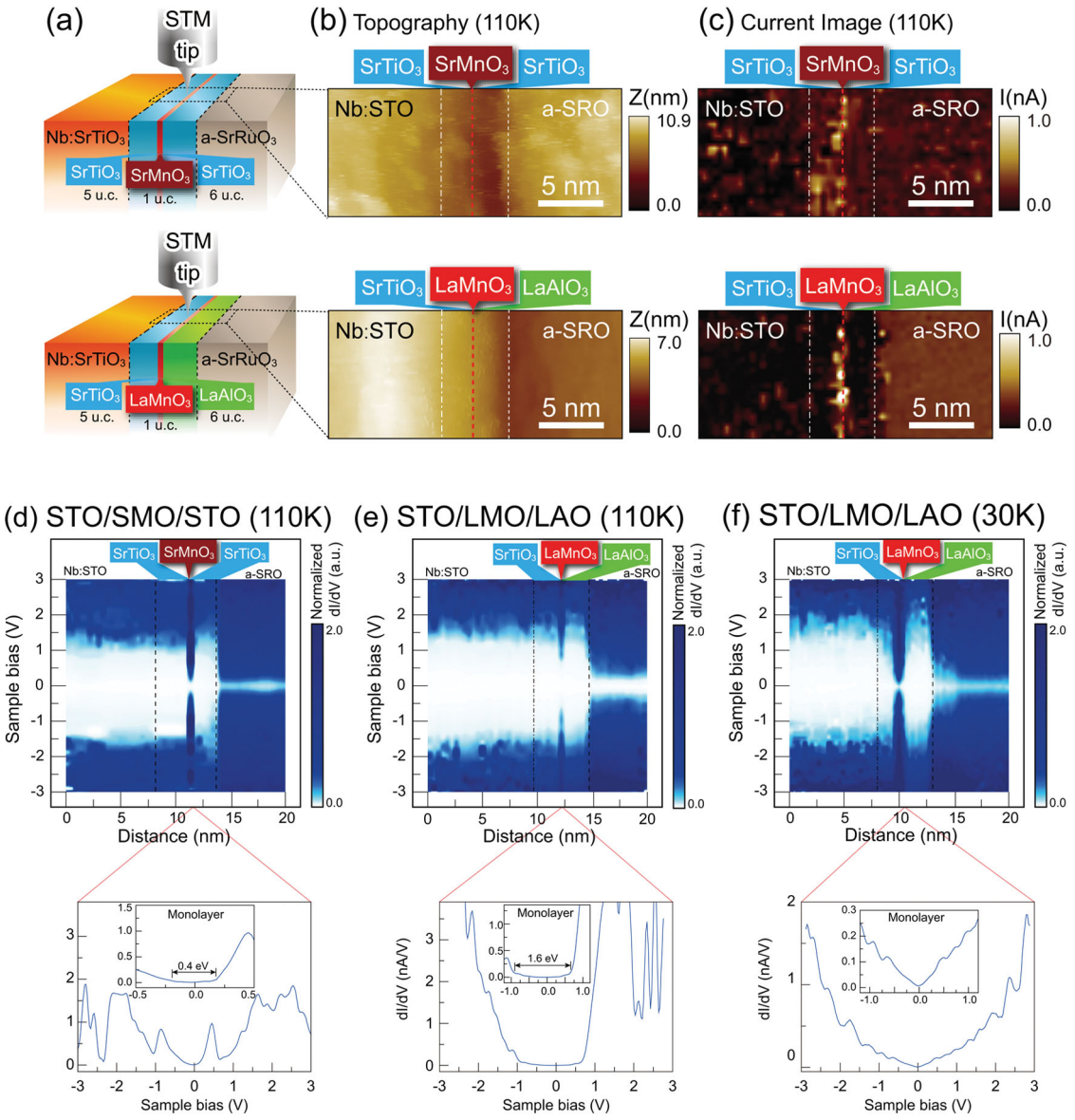

Figure 5. a) Schematics of cross-sectional STM employed to investigate the properties of the MnO_2 monolayers. b) Typical cross-sectional topography images of the case 1 and case 3 at sample bias of –2.0 V. c) STM/S spectroscopic current images of the case 1 and case 3 at sample bias of –2.0 V. The red dashed lines in case 1 and case 3 can be assigned as the position of the MnO_2 monolayers, which show brighter contrast compared to other region. d) Band alignment and the corresponding atomic-scale evolution of electronic properties across the MnO_2 monolayers in case 1 are measured at 110 K. e,f) The same analyses of case 3 are measured at 110 and 30 K, respectively.

band structure of case 3 was again measured at a lower temperature (30 K) and mapped in Figure 5f. A significant difference between the energy gap of the MnO_2 monolayer at 30 K (about zero) and at 110 K (about 1.6 eV) suggests that the MnO_2 monolayer in case 3 transits into the metallic state at low temperatures but in the semiconducting state at high temperatures, revealing a metal–insulator transition. Therefore, the results obtained from XSTM at low temperature qualitatively agreed to the DFT predictions. Moreover, such transition can also be correlated to the one found in the XMCD measurements.

To confirm the results of XAS-XMCD and XSTM measurements, we further carried out macroscopic electronic transport measurements. Due to the nature of high insulating states and the limitation of the instrument, the transport data of case 1 and case 2 are excluded. For case 3, a standard two-terminal transport measurement over the temperature range from 4.2 to 300 K was performed. The resistance versus temperature of case 3 is shown in **Figure 6**. The resistance decreases with increasing temperature in the temperature range from 60 to 300 K, exhibiting a semiconducting behavior. Such a semiconducting behavior can be described by several models such as localization and thermal excitation. The inset in Figure 6 shows that the logarithm of the conductance (G) of case 3 is linearly proportional to the temperature. Obviously, the transport

© 2016 WILEY-VCH Verlag GmbH & Co. KGaA, Weinheim

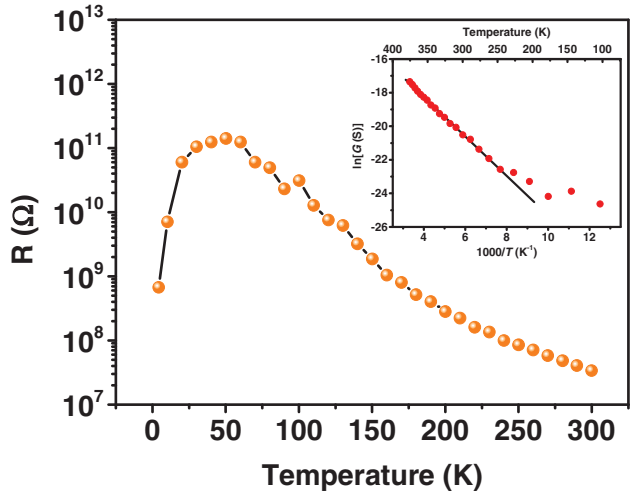

Figure 6. A metal–insulator transition with T_C around 70 K found in case 3 based on the result of resistance versus temperature. The inset is lnG as a function of temperature from 60 to 300 K for the case 3, in which the Arrhenius equation $G(T)$ can be well applied to fit the curve within this temperature range.

behavior in the insulating regime of case 3 follows Arrhenius equation $G(T) = G_0 \exp(E_A/K_BT)$ very well (G_0 is a prefactor of conductance). The thermal activation energy E_A to be about 170 meV was extracted. More importantly, a clear metal–insulator transition was observed at ≈60 K (Figure 6(a)), which is consistent with the observations from XSTM and XMCD measurements. To clarify the origin of conduction in case 3, a general 2DEG LAO/STO system with metallic behavior can be employed for comparison.[6–8] It has been known that the La-doping STO near the interface, resulting in the existence of Ti^{3+}, plays a crucial role in its high conductivity. However, in case 3, the presence of a mixed Mn valence states in the results of XAS, a typical signature of the metallic phase in manganite system, leads to the conduction of case 3. In addition, an abrupt drop of energy bandgap at interface within the length of ≈8 Å in the cross-sectional STM images as well as rare La cations at STO side near the interface in the STEM-EELS images indicate the limited cation intermixing of La and Mn cations with STO. Furthermore, no Ti^{3+} signal was detected in our system. Our previous study[34] that uses XSTM to characterize the electronic structure of LAO/STO interface also shows a significant difference of the band structure at the LAO/STO interface compared to case 3, precluding the contribution from STO. Therefore, we can conclude that the conduction mechanism in case 3 can be attributed to the MnO_2 monolayer, which is different from that induced by La-doping STO near the interface. Recall that the theoretical calculations show that the ground state is metal, which agrees with the experimental observation at low temperature as well. However, when the temperature reaches above T_C, i.e., the system enters a paramagnetic state, the system should behave more like an insulator attributed to the enhanced random spin scattering in paramagnetic state with local magnetic dipoles.[35,36]

In summary, we have successfully demonstrated that a sandwiched 2D metal-oxide monolayer can be fabricated by a precise control of the growth in atomic scale. The top capping layers, STO and LAO, provide the different electrostatic boundary conditions, which obviously influence the chemical, electronic, and magnetic states of the buried MnO_2 monolayers. Interestingly, the MnO_2 monolayer in case 3 is predicted to be a metal, which agrees with the experimental observation at low temperature. Moreover, an intriguing metal–insulator transition has been found to correlate with a magnetic transition in case 3. Therefore, the achievement of this study not only proposes a new concept to study the confinement of strongly correlated electrons in low dimension, but also offers the potential in modulating relevant novel phenomena in the domain of 2D strongly correlated electron systems.

Experimental Section

Sample Preparation: All samples were fabricated from stoichiometric targets (SMO, LMO, STO, and LAO) on the TiO_2-terminated STO (100) substrates using pulsed laser deposition equipping with a RHEED. During the deposition, the substrate temperature was maintained at 700 °C. The oxygen pressure was kept at 100 mTorr for the deposition of SMO, LMO, and STO. However, to avoid the possible 3D growth of LAO thin film, the pressure decreased to 5×10^{-5} Torr to ensure the layer-by-layer growth.[37] After the deposition, all the films were post-annealed at the oxygen pressure of ≈300 Torr for 30 min, and then cooled down to room temperature.

DFT Calculation: In the first-principles calculation within the framework of density-functional theory, the exchange-correlation potential is treated in local density approximation (LDA) and local density approximation plus Hubbard U (LDA+U) while the projected augmented wave method is used with a plane wave basis set as implemented in the Vienna ab initio simulation package (VASP).[38,39] A kinetic energy cut off is set to be 500 eV for the plane wave basis and the Brillouin zone integration for self-consistent field calculation is carried out using Monkhorst–Pack grid of $5\times5\times1$ k points for heterostructures and $8\times8\times8$ k points grid for bulk STO and LAO in combination with the tetrahedron method. The electronic self-consistency convergence is set to be 10^{-5} eV for all calculations. The optimized bulk lattice constants by LDA are 3.874 and 3.742 Å for STO and LAO, respectively, which are slightly underestimated with respect to their experimental values (3.905 and 3.789 Å) and are in agreement with Han's theoretical predictions.[40] In the optimization for the three cases, we fixed the in-plane lattice constant of the supercells at the relaxed lattice constant of bulk STO and performed relaxation of all the coordinates of atomic positions along the c-direction until the Hellmann–Feynman forces on each atom were less than 1 meV $Å^{-1}$. On account of the on-site electron–electron interactions in the localized 3d orbitals for Mn, we used LDA+U method introduced by Dudarev et al.[41] to get the Hamiltonian including screened Coulomb interactions. In order to investigate the effect on the Hamiltonian introduced by Hubbard correction, we carefully performed the calculations with the values U^{eff}_{Mn} = 2, 4, 4.5, and 7 eV, respectively, and the corresponding numerical data of exchange energy of Mn–Mn pair gained from total energy calculations were provided in the Supporting Information, Table S1. $\sqrt{2}\times\sqrt{2}\times13$ geometrical models were constructed to simulate the heterostructures. The qualitative results in our study are verified by both slab and superlattice models. Notably the slab model were simulated by adding imaginative vacuum thickness of 15 Å on top of capping layers and the dipole correction was included in calculations to eliminate the spurious field.

Structural Analysis by HAADF-STEM: A Cs-corrected STEM (JEM-2100F, JEOL, Co., Tokyo, Japan) operated at 200 kV and equipped with a spherical aberration corrector (CEOS Gmbh, Heidelberg, Germany) were performed with a minimum probe of about 1 Å in diameter. The probe convergence angle and the detection angle were 25 mrad and 92–228 mrad, respectively, during HAADF imaging. The low loss EELS analyses were carried out using a Cs-corrected STEM (JEM-ARM200F, JEOL,

© 2016 WILEY-VCH Verlag GmbH & Co. KGaA, Weinheim

Co., Tokyo, Japan) operated at 200 kV and equipped with a spherical-aberration corrector (CEOS GmbH, Heidelberg, Germany), a Gatan Image Filter (GIF), and a Wien-filter type monochromator. An entrance aperture of 2.5 mm was used and the energy resolution of 0.15 eV was determined by measuring the full-width half-maximum (FWHM) of the zero loss peak.

Magnetism Study by Soft X-Ray Absorption Techniques: The electronic structure and origin of magnetism of the MnO_2 monolayers were studied using soft XAS and XMCD at the Beamline I06 at Diamond and Dragon beamline at NSRRC. The temperature and magnetic field dependent spectra were recorded at the Mn $L_{2,3}$ edges (630–660 eV) with an energy resolution of 0.25 eV by shining Left (μ_+) and right (μ_-) circularly polarized X-rays on the samples. The measured temperature ranged from 3 K to room temperature. The applied magnetic field was performed from 0.2 to 6 T.

Cross-Section Scanning Tunneling Microscopy and Spectroscopy: Before the STM measurements, amorphous $SrRuO_3$ (SRO) capping layers (>500 nm) were deposited on top of all samples to prevent tip crash during the measurements. These samples were cleaved in situ in an UHV chamber whose base pressure was approximately 5×10^{-11} Torr. The cross-sectional STM topography images were obtained using constant current mode at −2.0 V. The corresponding atomically resolved spectroscopic results with the spatial resolution of 0.4 nm at interfaces were recorded with the first derivative of tunneling current over tip-sample voltage (or differential conductivity), dI/dV, at temperature of 30 and 110 K.

Electric transport Measurements: The typical transport measurement was performed on Cryogen-free 4 K cryogenic probe station (Lake Shore Model CRX-4K) with high resistance meter (Keithley Model 6517A) for the three cases samples. The conductance results, which are shown in this paper, are from inverse resistance, $G = 1/R$ and the resistance were obtained under the DC electric bias 1 V.

Supporting Information

Supporting Information is available from the Wiley Online Library or from the author.

Acknowledgements

The authors thank Dr. Takeharu Kato and Ryuji Yoshida at the Japan Fine Ceramics Center (JFCC) for their help in preparing TEM samples. The authors thank Prof. Wen-Bin Jian's laboratory for their assistance in the electric transport measurement. The authors acknowledge the support of the Ministry of Science and Technology under Grant No. MOST 103-2119-M-009-003-MY3. This work was also supported in part by the National Key Project for Basic Research of China (No. 2014CB921104 and 2013CB922301), the NSF of China (No. 61125403). It was also supported in part by Ministry of Science and Technology of Taiwan (Grant Ns. 103-2745-M-002-004-ASP). Computations in this work were performed at ECNU computing center and Chinese Tianhe-1A system at the National Supercomputer Center.

Received: April 29, 2016
Revised: July 10, 2016
Published online: August 29, 2016

[1] E. Dagotto, *Science* **2005**, *309*, 257.
[2] H. Takagi, H. Y. Hwang, *Science* **2010**, *327*, 1601.
[3] J. Mannhart, D. G. Schlom, *Science* **2010**, *327*, 1607.
[4] H. Y. Hwang, Y. Iwasa, M. Kawasaki, B. Keimer, N. Nagaosa, Y. Tokura, *Nat. Mater.* **2012**, *11*, 103.
[5] P. Zubko, S. Gariglio, M. Gabay, P. Ghosez, J.-M. Triscone, *Annu. Rev. Condens. Matter Phys.* **2011**, *2*, 141.
[6] A. Ohtomo, H. Y. Hwang, *Nature* **2004**, *427*, 423.
[7] N. Reyren, S. Thiel, A. D. Caviglia, L. F. Kourkoutis, G. Hammerl, C. Richter, C. W. Schneider, T. Kopp, A.-S. Rüetschi, D. Jaccard, M. Gabay, D. A. Muller, J.-M. Triscone, J. Mannhart, *Science* **2007**, *317*, 1196.
[8] A. D. Caviglia, S. Gariglio, C. Cancellieri, B. Sacépé, A. Fête, N. Reyren, M. Gabay, A. F. Morpurgo, J. M. Triscone, *Phys. Rev. Lett.* **2010**, *105*, 236802.
[9] L. Li, C. Richter, S. Paetel, T. Kopp, J. Mannhart, R. C. Ashoori, *Science* **2011**, *332*, 825.
[10] A. D. Caviglia, S. Gariglio, N. Reyren, D. Jaccard, T. Schneider, M. Gabay, S. Thiel, G. Hammerl, J. Mannhart, J. M. Triscone, *Nature* **2008**, *456*, 624.
[11] A. D. Caviglia, M. Gabay, S. Gariglio, N. Reyren, C. Cancellieri, J. M. Triscone, *Phys. Rev. Lett.* **2010**, *104*, 126803.
[12] B. Radisavljevic, A. Radenovic, J. Brivio, V. Giacometti, A. Kis, *Nat. Nanotechnol.* **2011**, *6*, 147.
[13] W. S. Yun, S. W. Han, S. C. Hong, I. G. Kim, J. D. Lee, *Phys. Rev. B* **2012**, *85*, 033305.
[14] A. Kuc, N. Zibouche, T. Heine, *Phys. Rev. B* **2011**, *83*, 245213.
[15] K. S. Novoselov, A. K. Geim, S. V. Morozov, D. Jiang, Y. Zhang, S. V. Dubonos, I. V. Grigorieva, A. A. Firsov, *Science* **2004**, *306*, 666.
[16] B. Keimer, S. A. Kivelson, M. R. Norman, S. Uchida, J. Zaanen, *Nature* **2015**, *518*, 179.
[17] Y. Maeno, H. Hashimoto, K. Yoshida, S. Nishizaki, T. Fujita, J. G. Bednorz, F. Lichtenberg, *Nature* **1994**, *372*, 532.
[18] A. Gozar, G. Logvenov, L. F. Kourkoutis, A. T. Bollinger, L. A. Giannuzzi, D. A. Muller, I. Bozovic, *Nature* **2008**, *455*, 782.
[19] Y. Z. Chen, F. Trier, T. Wijnands, R. J. Green, N. Gauquelin, R. Egoavil, D. V. Christensen, G. Koster, M. Huijben, N. Bovet, S. Macke, F. He, R. Sutarto, N. H. Andersen, J. A. Sulpizio, M. Honig, G. E. D. K. Prawiroatmodjo, T. S. Jespersen, S. Linderoth, S. Ilani, J. Verbeeck, G. Van Tendeloo, G. Rijnders, G. A. Sawatzky, N. Pryds, *Nat. Mater.* **2015**, *14*, 801.
[20] T. Kimura, Y. Tomioka, H. Kuwahara, A. Asamitsu, M. Tamura, Y. Tokura, *Science* **1996**, *274*, 1698.
[21] Y. Moritomo, A. Asamitsu, H. Kuwahara, Y. Tokura, *Nature* **1996**, *380*, 141.
[22] M. B. Salamon, M. Jaime, *Rev. Mod. Phys.* **2001**, *73*, 583.
[23] M. Kawasaki, K. Takahashi, T. Maeda, R. Tsuchiya, M. Shinohara, O. Ishiyama, T. Yonezawa, M. Yoshimoto, H. Koinuma, *Science* **1994**, *266*, 1540.
[24] S. Clarke, D. D. Vvedensky, *Phys. Rev. Lett.* **1987**, *58*, 2235.
[25] T. Terashima, Y. Bando, K. Iijima, K. Yamamoto, K. Hirata, K. Hayashi, K. Kamigaki, H. Terauchi, *Phys. Rev. Lett.* **1990**, *65*, 2684.
[26] Y. Z. Chen, N. Bovet, T. Kasama, W. W. Gao, S. Yazdi, C. Ma, N. Pryds, S. Linderoth, *Adv. Mater.* **2014**, *26*, 1462.
[27] G. Trimarchi, N. Binggeli, *Phys. Rev. B* **2005**, *71*, 035101.
[28] M. Cococcioni, S. de Gironcoli, *Phys. Rev. B* **2005**, *71*, 035105.
[29] K. W. Edmonds, N. R. S. Farley, T. K. Johal, G. van der Laan, R. P. Campion, B. L. Gallagher, C. T. Foxon, *Phys. Rev. B* **2005**, *71*, 064418.
[30] T. Burnus, Z. Hu, H. H. Hsieh, V. L. J. Joly, P. A. Joy, M. W. Haverkort, H. Wu, A. Tanaka, H. J. Lin, C. T. Chen, L. H. Tjeng, *Phys. Rev. B* **2008**, *77*, 125124.
[31] C. Aruta, G. Ghiringhelli, V. Bisogni, L. Braicovich, N. B. Brookes, A. Tebano, G. Balestrino, *Phys. Rev. B* **2009**, *80*, 014431.
[32] R. Loetzsch, A. Lübcke, I. Uschmann, E. Förster, V. Große, M. Thuerk, T. Koettig, F. Schmidl, P. Seidel, *Appl. Phys. Lett.* **2010**, *96*, 071901.

© 2016 WILEY-VCH Verlag GmbH & Co. KGaA, Weinheim

[33] B. Subhankar, K. Wolfgang, *J. Phys. D: Appl. Phys.* **2009**, *42*, 013001.
[34] B.-C. Huang, Y.-P. Chiu, P.-C. Huang, W.-C. Wang, V. T. Tra, J.-C. Yang, Q. He, J.-Y. Lin, C.-S. Chang, Y.-H. Chu, *Phys. Rev. Lett.* **2012**, *109*, 246807.
[35] *Modern Trends in Magnetostriction Study and Application* (Ed: M. R. J. Gibbs), Kluwer Academic Publishers, USA **2001**, p. 213.
[36] *Magnetism and Structure in Functional Materials* (Eds: A. Planes, L. Mañosa, A. Saxena), Springer, Berlin, **2005**, p. 76.
[37] Ariando, X. Wang, G. Baskaran, Z. Q. Liu, J. Huijben, J. B. Yi, A. Annadi, A. R. Barman, A. Rusydi, S. Dhar, Y. P. Feng, J. Ding, H. Hilgenkamp, T. Venkatesan, *Nat. Commun.* **2011**, *2*, 188.
[38] G. Kresse, J. Hafner, *Phys. Rev. B* **1993**, *47*, 558.
[39] G. Kresse, J. Hafner, *Phys. Rev. B* **1994**, *49*, 14251.
[40] Y.-L. Han, Y.-W. Fang, Z.-Z. Yang, C.-J. Li, L. He, S.-C. Shen, Z.-Z. Luo, G.-L. Qu, C.-M. Xiong, R.-F. Dou, X. Wei, L. Gu, C.-G. Duan, J.-C. Nie, *Phys. Rev. B* **2015**, *92*, 115304.
[41] S. L. Dudarev, G. A. Botton, S. Y. Savrasov, C. J. Humphreys, A. P. Sutton, *Phys. Rev. B* **1998**, *57*, 1505.

© 2016 WILEY-VCH Verlag GmbH & Co. KGaA, Weinheim